

## Research article

Wei Zhu, Ruisheng Yang, Guangzhou Geng, Yuancheng Fan, Xuyue Guo, Peng Li, Quanhong Fu, Fuli Zhang\*, Changzhi Gu\* and Junjie Li\*

# Titanium dioxide metasurface manipulating high-efficiency and broadband photonic spin Hall effect in visible regime

<https://doi.org/10.1515/nanoph-2020-0290>

Received May 15, 2020; accepted July 21, 2020; published online August 6, 2020

**Abstract:** The interactions of photonic spin angular momentum and orbital angular momentum, i.e., the spin-orbit coupling in focused beams, evanescent waves or artificial photonic structures, have attracted intensive investigations for the unusual fundamental phenomena

**Wei Zhu, Ruisheng Yang and Guangzhou Geng:** These authors contributed equally to this work.

**\*Corresponding authors:** Fuli Zhang, Key Laboratory of Space Applied Physics and Chemistry, Ministry of Education and Department of Applied Physics, School of Science, Northwestern Polytechnical University, Xi'an 710129, China; and School of Physical Science and Technology and Shenzhen Research and Development Institute, Northwestern Polytechnical University, Xi'an, 710129, China, E-mail: fuli.zhang@nwpu.edu.cn; and Changzhi Gu, Beijing National Laboratory for Condensed Matter Physics, Institute of Physics, Chinese Academy of Sciences, Beijing, 100190, China; and School of Physical Sciences, CAS Key Laboratory of Vacuum Physics, University of Chinese Academy of Sciences, Beijing, 100049, China, E-mail: czgu@iphy.ac.cn; and Junjie Li, Beijing National Laboratory for Condensed Matter Physics, Institute of Physics, Chinese Academy of Sciences, Beijing, 100190, China; and School of Physical Sciences, CAS Key Laboratory of Vacuum Physics, University of Chinese Academy of Sciences, Beijing, 100049, China; and Songshan Lake Materials Laboratory, Dongguan, Guangdong, 523808, China, E-mail: jjli@iphy.ac.cn

**Wei Zhu,** Beijing National Laboratory for Condensed Matter Physics, Institute of Physics, Chinese Academy of Sciences, Beijing, 100190, China; and School of Physical Science and Technology and Shenzhen Research and Development Institute, Northwestern Polytechnical University, Xi'an, 710129, China. <https://orcid.org/0000-0003-0673-3048>

**Ruisheng Yang, Yuancheng Fan, Xuyue Guo, Peng Li and Quanhong Fu,** School of Physical Science and Technology and Shenzhen Research and Development Institute, Northwestern Polytechnical University, Xi'an, 710129, China. <https://orcid.org/0000-0002-7919-4148> (Y. Fan). <https://orcid.org/0000-0001-8780-5554> (P. Li)

**Guangzhou Geng,** Beijing National Laboratory for Condensed Matter Physics, Institute of Physics, Chinese Academy of Sciences, Beijing, 100190, China

in physics and potential applications in optical and quantum systems. It is of fundamental importance to enhance performance of spin-orbit coupling in optics. Here, we demonstrate a titanium dioxide (TiO<sub>2</sub>)-based all-dielectric metasurface exhibiting a high efficient control of photonic spin Hall effect (PSHE) in a transmissive configuration. This metasurface can achieve high-efficiency symmetric spin-dependent trajectory propagation due to the spin-dependent Pancharatnam-Berry phase. The as-formed metadevices with high-aspect-ratio TiO<sub>2</sub> nanofins are able to realize (86%, measured at 514 nm) and broadband PSHEs in visible regime. Our results provide useful insights on high-efficiency metasurfaces with versatile functionalities in visible regime.

**Keywords:** high-efficiency metasurface; photonic spin Hall effect; spin-dependent trajectory propagation; spin-orbit coupling.

## 1 Introduction

Spin Hall effect (SHE) is the physical phenomenon associated with the spin-dependent trajectories of electric current due to spin-orbit interaction (SOI) [1–3]. Photonic spin Hall effect (PSHE) is the photonic analogy of SHE which refers to the transverse spin-split of light trajectory [4–7]. The transverse splitting of trajectory of light originates from the opposite geometric phases for the two spins/polarizations through the interactions of photonic spin angular momentum and orbital angular momentum [8, 9]. The spin-orbit coupling is rising as a promising platform for novel photonic functions such as beam generator and detectors, hologram, polarization control and lens [10, 11]. In that it is highly desirable to achieve high efficient control of spin-orbital coupling especially in visible regime, where many medium including noble metals and silicon show nonignorable damping. Furthermore, it has provided new degrees of freedom to control spin photonics and is

potentially useful for exploiting multifunctional spin photonics devices.

Recently, metamaterial with rationally designed building blocks have enabled the realization of many phenomena and functionalities unavailable through use of naturally occurring materials [12–16]. Many basic and anisotropic metamaterial structures, such as metal splitting resonators, exhibit birefringence suitable for polarization conversion [17–24]. Metasurfaces, the two-dimensional counterpart of the metamaterials have also been developed for high-efficiency light manipulations [25–37]. Compared to metamaterials composed of complex three-dimensional structures, metasurfaces can be easily fabricated by using the photolithography or nanoprinting. As the operation wavelength goes to the optical regime, metasurfaces made of metals are always suffered from the severe ohmic loss, which usually results in high damping and low efficiency, especially in transmissive metasurfaces.

All-dielectric metasurfaces with building blocks of high-refractive and low-loss dielectrics have been proposed as an alternative route, where the ohmic damping could be avoided [38–47]. Most of the all-dielectric metasurfaces demonstrated so far are made of silicon because it is compatible with current fabrication processing technology. The dielectric loss of silicon is negligible in terahertz and infrared regime, while it increases rapidly at visible wavelength [48]. The titanium dioxide ( $\text{TiO}_2$ ) has emerged as a promising candidate for manipulating visible light with high-efficiency over nanoscale dimensions because its refractive index ( $\sim 2.5$ ) is high and dielectric loss ( $\sim 0$ ) is negligible at visible wavelength [49], which is suitable for fabricating high-efficiency and broadband dielectric metasurfaces in visible regime [48–53].

In this work, we propose and experimentally demonstrate an all-dielectric metasurface capable of achieving high-efficiency and broadband PSHE with a transmissive configuration in visible regime. The PSHE is arising from the opposite geometric Pancharatnam-Berry phases of two spins in polarization space. Compared to the silicon metasurfaces with aspect-ratio (1:3) Si nanofins, the metasurface with building blocks of rationally rotated high-aspect-ratio (1:7.5)  $\text{TiO}_2$  nanofins standing on a quartz substrate is fabricated through highly precise electron beam lithography (EBL) and atomic layer deposition (ALD) procedures. The  $\text{TiO}_2$ -based dielectric metasurface shows a symmetric transverse spin-dependent trajectory of transmitted left-handed circular polarization (LCP) and right-handed circular polarization (RCP) with high efficiency (97.6% [calculated] and 86% [measured] at wavelength 514 nm) due to the strong SOI. It is also found that the metasurface can realize high-efficiency spin-dependent photonic functions in a broadband manner. The proposed SOI metasurface is miniaturized to subwavelength scale and increases additional internal degrees of freedom, which is promising in future integrated on-chip devices with multichannel information processing.

## 2 Results and discussion

Figure 1A shows the designed transmissive all-dielectric metasurface that exhibits transverse spin-dependent trajectories due to the SOI in a broadband manner. The building blocks of our metasurface are high-aspect-ratio  $\text{TiO}_2$  nanofins (Figure 1B) standing on a quartz substrate. The required phase is imparted by rotation of nanofin by an angle  $\theta$  based on the geometric Pancharatnam-Berry phase. To split the two spins (LCP and RCP) in the

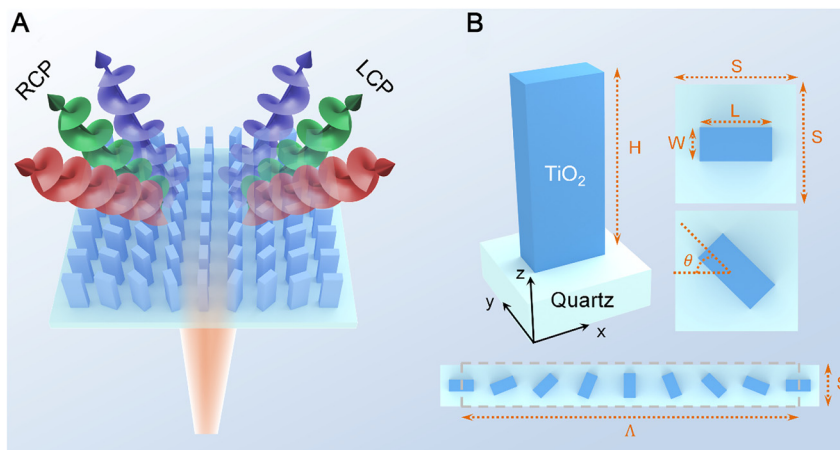


**Figure 1:** Design of a metasurface exhibiting high-efficiency PSHE. **(A)** Schematic diagram of the metasurface showing spin-splitting, and its building block of  $\text{TiO}_2$  nanofins on a quartz substrate. **(B)** Side and top views of the supercell of nanofin grating with periodic dimension  $\Lambda \times S$ . Each supercell consists of eight nanofin elements. Top views of a nanofin showing width  $W$ , length  $L$  with unit cell dimension  $S \times S$  and the rotation of nanofin by an angle  $\theta$  results in the required phase (geometric Pancharatnam-Berry phase). Side view of a  $\text{TiO}_2$  nanofin on a quartz substrate showing height  $H$ . Incident plane wave propagates along the  $z$  direction. The geometric parameters are:  $\Lambda = 3120$  nm,  $S = 390$  nm,  $W = 80$  nm,  $L = 230$  nm,  $H = 600$  nm. PSHE, photonic spin Hall effect.

transverse of light trajectory, the phase profile  $\varphi$  of the metasurface needs to follow

$$\varphi(x) = \pm \frac{2\pi}{\lambda} \times \frac{x}{\Lambda} \quad (1)$$

where  $\lambda$  is the design wavelength,  $x$  is the coordinate of each nanofin,  $\Lambda$  is the periodic dimension of each supercell, and the sign of “ $\pm$ ” is for RCP (LCP) incidence. This phase profile is acquired by rotating each nanofin by an angle

$$\theta(x) = \frac{\pi}{\lambda} \times \frac{x}{\Lambda} \quad (2)$$

In our metasurface, every eight nanofins that rotate by  $\theta = 1/8\pi$  make up a supercell with periodic dimension  $\Lambda \times S$ . In order to achieve the maximum polarization conversion efficiency (PCE), every nanofin with birefringence originating from the asymmetric cross section is supposed to operate as a half-waveplate. We measured the optical constant of  $\text{TiO}_2$  film by utilizing ellipsometer (see Figure S1 in the supplementary material) and employed a finite difference time domain (FDTD) method for investigating the birefringence effect. The PCE under several different illumination wavelengths were firstly determined via simulations as functions of the length and width of the nanofin (see Figure S2 in the supplementary material). Since the results for parameter  $L = 230$  nm and  $W = 80$  nm exhibit high efficiency in a broadband manner, we select these optimized parameters to further design and fabricate the metasurface. The simulated PCE can be greater than 90% in a broad wavelength ranging from 502 to 528 nm and as high as 98% in the desired wavelength 514 nm (Figure 2A), indicating the high-efficiency and broadband performance of the  $\text{TiO}_2$ -based photonic device. Displacement electric field distribution for  $x$ -component (Figure 2B) and  $y$ -component (Figure 2C) in a nanofin at the wavelength 514 nm under circular polarization (CP) illumination show

that a phase retardation between the  $x$  and  $y$  polarizations as  $\pi$  can be achieved, further confirming the role of  $\text{TiO}_2$  nanofin as a half-waveplate. For these simulations, periodic boundary conditions are applied at the  $x$  and  $y$  directions and perfectly matched layers (PMLs) are applied at the  $z$  directions. We calculate the PCE as the ratio of the transmitted opposite helicity power to the incident power.

For normal incidence of CP light, the transmitted electric field ( $E_{L/R}^t$ ) of the nanofin rotated by an angle  $\theta$  (Figure 1b) can be deduced through Jones matrix as follows [54]:

$$E_{L/R}^t = \frac{e^{i\phi/2} + e^{-i\phi/2}}{2} \hat{e}_{L/R} + \frac{e^{i\phi/2} - e^{-i\phi/2}}{2} e^{\pm i2\theta} \hat{e}_{R/L} \quad (3)$$

where  $\phi$  represents the phase retardation between the length and width of the nanofin along the propagating direction,  $\hat{e}_{L/R} = (\hat{e}_x \pm i\hat{e}_y)/\sqrt{2}$  is the Jone's vector of LCP or RCP. The two terms in Equation (3) represent the transmitted CP waves with the same and opposite helicity compared to the incident wave, respectively. Note that the opposite helicity radiation carries an additional phase delay of  $\varphi = \pm 2\theta$ , which is known as Pancharatnam-Berry phase and is crucial for constructing a metasurface with phase gradient. The signs of “ $+$ ” and “ $-$ ” are for RCP and LCP incidence, respectively. This spin-dependent Pancharatnam-Berry phase in the polarization space leads to the opposite trajectory of the two spins, resulting in spin-splitting and PSHE. The transmitted phase can be tuned from 0 to  $\pm 2\pi$  as the nanofin is rotated from 0 to  $\pi$ . In our metasurface, the  $\phi$  is approximately equal to  $\pi$  at the wavelength 514 nm. Therefore, the transmitted electric field ( $E_{L/R}^t$ ) can be expressed as  $E_{L/R}^t = ie^{\pm i2\theta} \hat{e}_{R/L}$ , indicating that nearly total incident CP light is converted into opposite handedness radiation.

To construct our metasurface, 8-phase levels from 0 to  $2\pi$  with  $1/8\pi$  step under RCP normal incidence were chosen as shown in Figure 3A. According to wave vectors

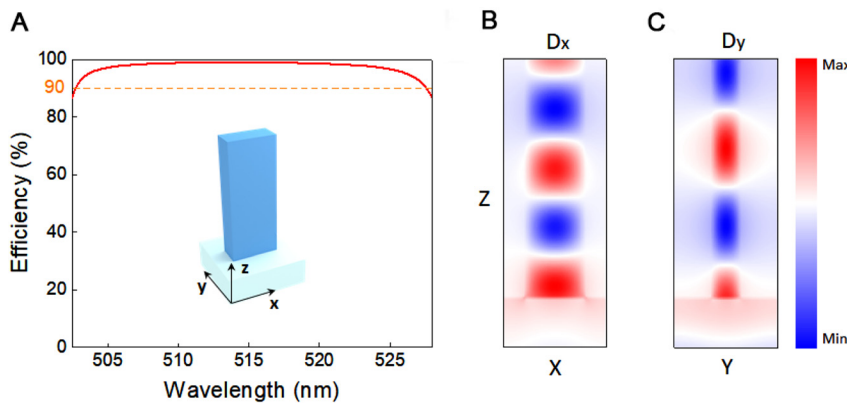


**Figure 2:** Birefringence effect of a  $\text{TiO}_2$  nanofin metasurface. **(A)** Simulated and measured polarization conversion efficiency as a function of wavelength. **(B and C)** Simulated displacement electric field ( $x$ -component and  $y$ -component) distribution in a nanofin at the wavelength 514 nm with circular polarization illumination.

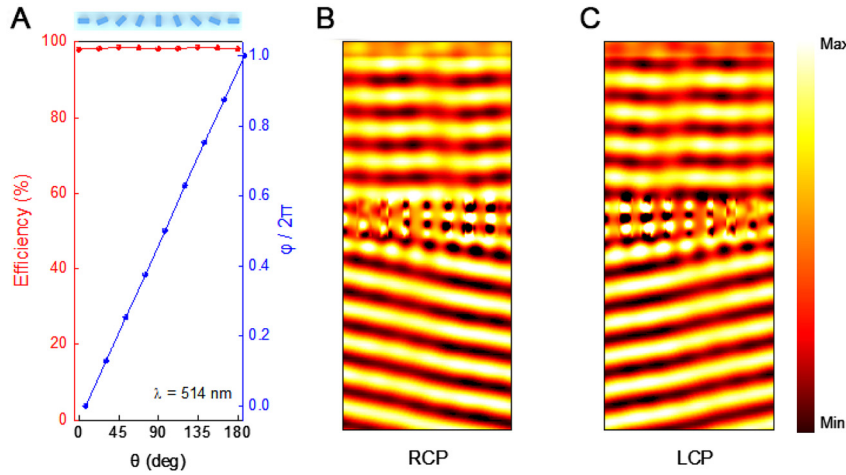


**Figure 3:** Angular dependence of phase and polarization conversion efficiency of nanofin and electric field maps. **(A)** Simulated polarization conversion efficiency (red points) and phase (blue points) of a nanofin with  $\theta$  varying from  $0^\circ$  to  $180^\circ$ . **(B and C)** Simulated electric field maps for RCP and LCP illumination, respectively.

momentum conservation law, the refraction can be expressed as generalized Snell's law:

$$k_{t,x} = k_{i,x} \pm \frac{\partial\varphi}{\partial x} \quad (4)$$

where  $k_{t,x}$  and  $k_{i,x}$  represent the  $x$ -component of the incident and transmitted transverse wave vector, and  $\pm \partial\varphi/\partial x$  is the spin-dependent phase gradient (here the sign “ $\pm$ ” for RCP (LCP) incidence). This spin-dependent phase gradient can cause the spin-dependent orbit angular momentum. To conserve the total angular momentum, the orbit angular momentum along the  $z$  direction will be reduced due to the SOI. It is significant that the sign of the phase profile will be totally flipped if the helicity of the incident CP light is changed to the opposite one, which is critical to achieve a transverse spin-split of light trajectory. The electric field maps in Figure 3B and C shows that the incident RCP and LCP are refracted in two symmetric angular directions, further confirming the spin-dependent trajectory propagation. This angle of refraction can be calculated by the generalized Snell's law as  $\theta' = \sin^{-1}\left(\frac{\partial\varphi/\partial x}{2\pi/\lambda}\right) = \sin^{-1}\left(\frac{\lambda}{\Lambda}\right) = 9.48^\circ$ . Since the geometric phases of the two spins are opposite, the proposed metasurface supports a symmetric spin-splitting of the propagating direction under linear polarization (LP) illumination with normal incidence.

## 2.1 Metasurface fabrication and far-field measurements

Scanning electron micrograph (SEM) of the fabricated  $\text{TiO}_2$  metasurface is shown in Figure 4. The top view SEM of the fabricated metasurface is presented in Figure 4A, where an enlarged supercell is denoted by a dashed red rectangular.

Correspondingly, Figure 4B shows the side view SEM of the fabricated metasurface, in which the high-aspect-ratio  $\text{TiO}_2$  nanofins are clearly displayed. The as-fabricated  $\text{TiO}_2$  nanofins metasurface agrees well with the design, and the detailed fabrication process is described in Methods Section.

Figure 4C–E shows the comparison of far-field intensity distributions between simulation and experiment under LP, RCP and LCP illumination with normal incidence. The LP light can be considered as the superposition state of LCP and RCP. These two spins will be refracted into transverse symmetric propagating directions after passing through the metasurface. Under LP illumination (Figure 4C), as expected, the transmitted wave is splitted into two symmetric angular direction of  $m = -1$  and  $m = +1$ , respectively. The transmitted power of  $m = -1$ ,  $m = 0$  and  $m = +1$  orders are 48.8, 0.4 and 48.8% in simulation, and 42.6, 0.09 and 43.4% in experiment. For RCP illumination (Figure 4D), the simulated (measured) power of  $m = 0$  does not change but the  $m = +1$  order increases to 97.6% (86%) while the  $m = -1$  decreases to 0%, indicating the high-efficiency PSHE of our metasurface. The simulated trend agrees well with the measured results. For LCP illumination (Figure 4E), we can observe opposite trend. The simulated (measured) power of  $m = 0$  does not change but the  $m = -1$  order increases to 97.6% (86%) while the  $m = +1$  decreases to 0%. The reason that the measured efficiency cannot reach to the expected value in simulation is mainly due to the inevitable imperfection in device fabrication. These simulations are performed using the FDTD method for a supercell of eight nanofins with periodic conditions along  $x$  and  $y$  directions and PML long  $z$  directions. It is worth mentioning that the high-efficiency PSHE can also be achieved in a broadband manner. To further confirm the

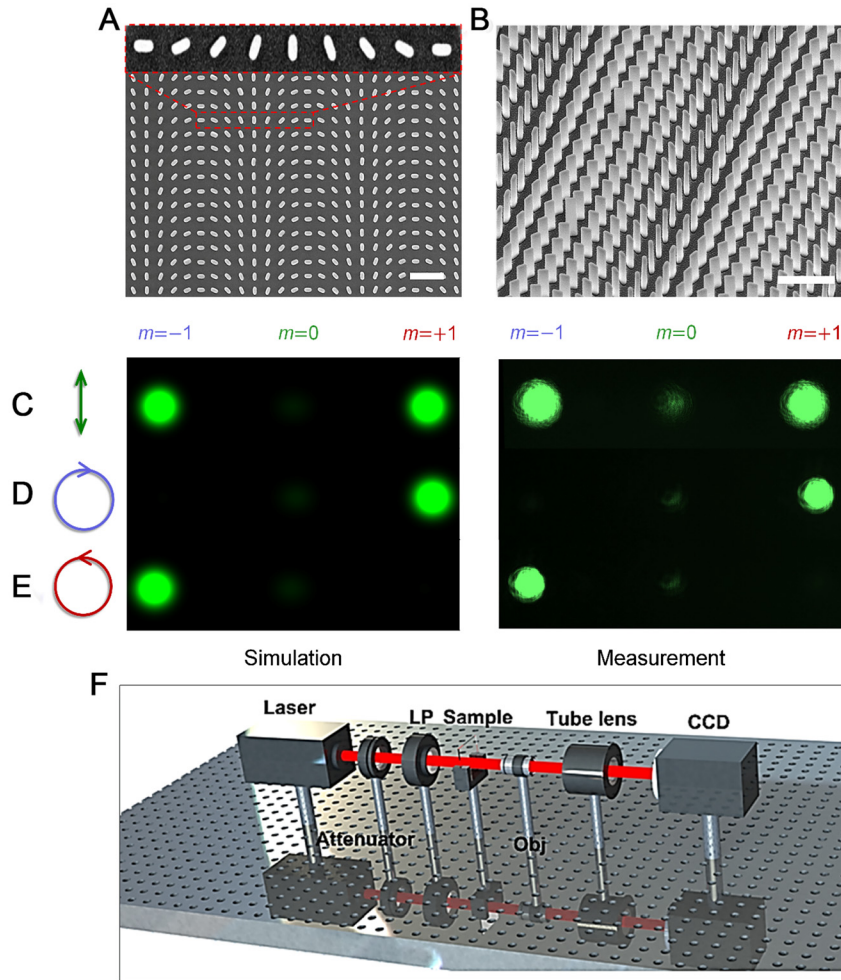


**Figure 4:** Fabricated titanium dioxide metasurface and comparison between simulations and measurements with different polarization states illumination at 514 nm. Scanning electron micrograph (SEM) of a fabricated metasurface, top (A) and side (B) view, and an enlarged image of the supercell is marked and inserted in (A). Simulated and measured far-field intensity profiles of  $m = -1$ ,  $m = 0$  and  $m = +1$  orders with incident polarization states of (C) LP, (D) RCP and (E) LCP, respectively. (F) Optical measurement setup for the metasurface, consisting of a laser with desired wavelength whose beam is passing through a linear polarizer and a quarter-waveplate to generate the input light with desired polarization to illuminate the metasurface, and the transmission light is measured by a charge-coupled device (CCD) camera. Scale bar: 1  $\mu\text{m}$ .

spin-dependent splitting of the PSHE, the Stokes parameter  $S_3$  was also measured in experiment (see Figure S3 and Note 3 in the supplementary material). The opposite spin accumulation is observed for the two symmetric angular direction of  $m = -1$  and  $m = +1$ . Figure 4F shows the optical measuremental setup to test far-field intensity distributions of our fabricated metasurface, and the related descriptions are given in Methods Section.

We characterized the working performance of the metasurface under several different illumination wavelengths, as shown in Figure 5A. The incident beam can be splitted with larger offset with the wavelength increasing from 450 to 670 nm. Figure 5B showed the results for the beam-centroid shift versus transimission distance under different illumination wavelength according to generalized Snell's law. As the wavelength increases from 450 to 670 nm, the beam-centroid shift increases correspondingly. This trend agrees well with measured results shown

in Figure 5A. Note that the metasurface can exhibit high-efficiency and broadband PSHE for almost the entire visible regime from 450 to 670 nm. We measured the working efficiency for several discrete illumination wavelengths of 450, 488, 532, 633 and 670 nm, and the corresponding efficiencies are 33.6, 50.0, 78.7, 73.9 and 62.6%, respectively. The detailed measured power intensities are shown in Figure 5C.

### 3 Conclusions

In summary, we have demonstrated a titanium dioxide based all-dielectric metasurface capable of realizing high-efficiency and broadband PSHE in visible regime. The metasurface composed of high-aspect-ratio  $\text{TiO}_2$  nanofins with spatially variant orientation was perfectly fabricated on a quartz substrate. Under LP, LCP and RCP illuminations, we found that this metasurface enabled spin-dependent

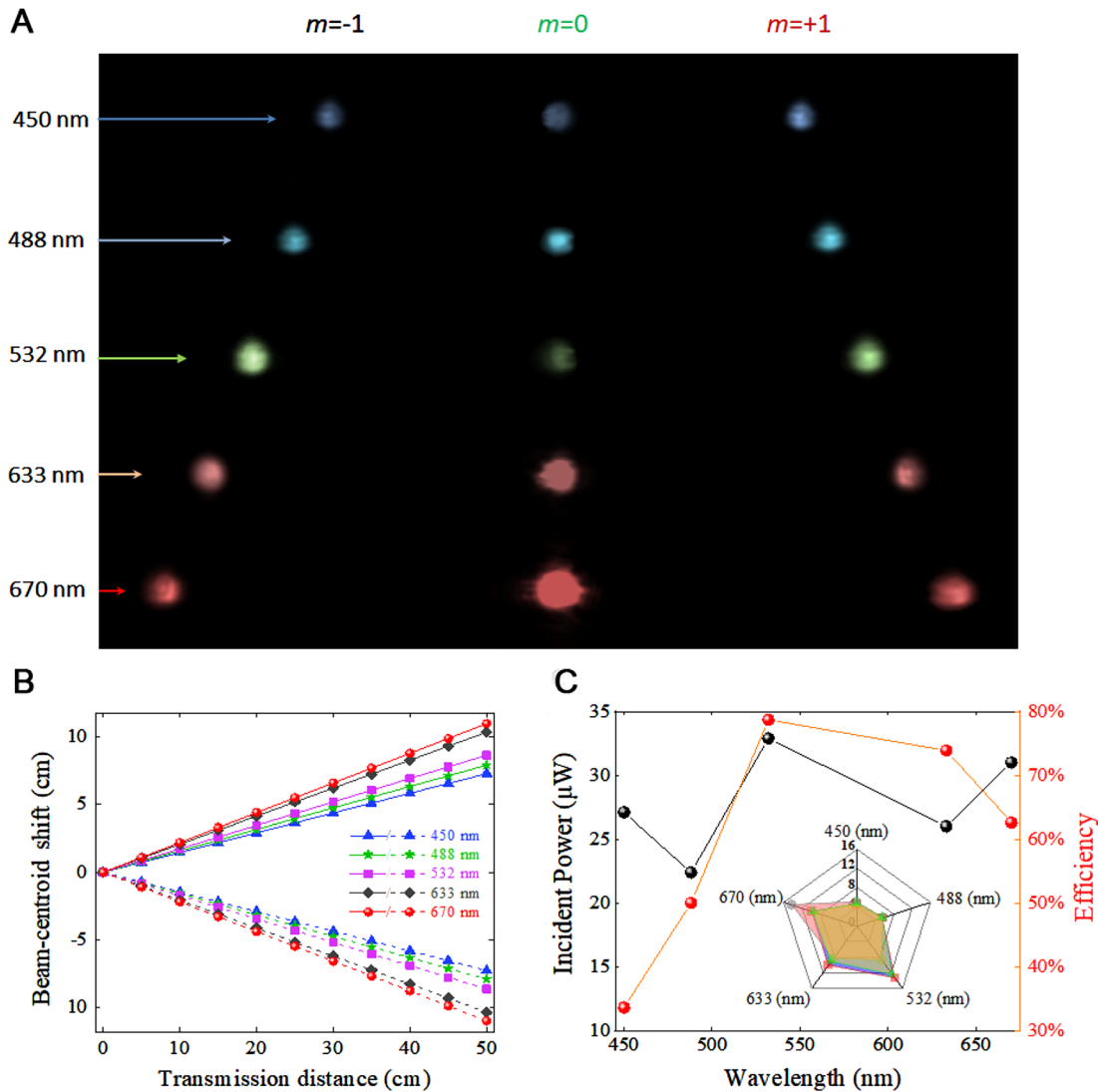


**Figure 5:** Broadband performance of the metasurface. **(A)** Experimentally measured far-field intensity distributions in linear scale, where false colors correspond to their respective wavelengths. **(B)** Calculated results for the beam-centroid shift versus transmission distance with different illumination wavelength. **(C)** Measured incident power intensity and operating efficiency under different illumination wavelengths. The inset shows the transmitted power intensity for each diffraction orders  $m = 0$  (gray points and red area),  $m = -1$  (red points and blue area) and  $m = +1$  (green points and yellow area) with different illumination wavelength.

propagation due to the opposite geometric Pancharatnam-Berry phases in polarization space. The designed and measured maximum operating efficiencies (at  $\lambda = 514$  nm) reach up to 97.6 and 86%, respectively. Moreover, high-efficiency PSHE can also be achieved in a broadband manner for almost entire visible regime. The controllable manipulation of strong SOI of light with tailored nanofins paves the avenue to spin-controlled photonics devices, which promises important applications in optical communications, quantum information processing and photonic devices in the future.

## 4 Methods

### 4.1 Sample fabrication

The metasurface samples were fabricated on a 500- $\mu\text{m}$ -thick quartz wafer. After cleaning the quartz wafer with acetone and isopropyl alcohol, a layer of positive electron beam resist (EBR) (PMMA; 495A5) with a thickness of 600 nm was spin-coated on the substrate, followed by baking for 1 min at 180° on a hot plate. A thin layer of conductive polymer Spacer was then spin-coated to avoid charging effects during the writing process. Next, rectangle-shaped nanostructure patterns were defined on the resist layer by

EBL on a JEOL 6300FS system (100 kV, 100 pA) with a dose area of  $1100 \mu\text{C}/\text{cm}^2$ . The patterned area was  $200 \times 200 \mu\text{m}^2$ . In this way, the process of EBL will cost 30 min per patterned area. After EBL, the Spacer was developed in MIBK:IPA = 1:3 for 3 min under gentle agitation and removed by water rinsing. The  $\text{TiO}_2$  was deposited directly onto the exposed EBR through ALD. A standard two-pulse system of water and tetrakis (dimethylamido) titanium(IV) (TDMAT) precursor was employed with a 0.015 s water pulse followed by a 20 s delay and a 0.4 s TDMAT pulse followed by a 20 s delay. The system was left under continuous 20 sccm flow of  $\text{N}_2$  carrier gas and was maintained at  $105^\circ\text{C}$  throughout the process. This led to an overall deposition rate of 0.6 nm per cycle. So, the process of ALD will cost 16 h to fill the nanostructures up. This process ultimately leaves a blanket film of  $\text{TiO}_2$  covering the entire device which must be removed to expose the individual metasurface units. This film was removed with reactive ion etching using a mixture of  $\text{Cl}_2$ ,  $\text{BCl}_3$  and Ar gas (20, 6 and 5 sccm, respectively) at a pressure of 4 mTorr, substrate bias of 150 V, inductively coupled plasma power of 400 W. Etch rates were typically between 1.3 and 1.6 nm/s. According to the thickness of the entire titanium oxide film, it is estimated that the entire etching process takes only 2 min. After processing was completed, the resist was removed by placing the samples in PG Remover for 24 h, followed by a final clean in 2:1, sulfuric acid: $\text{H}_2\text{O}_2$ . Due to many complicated processes of fabrication, it will take at least 60 h to finish the entire sample. And there is no doubt that the high-aspect-ratio characteristic of nanofin brings a huge challenge to the success rate of sample fabrication. Considering the above factors comprehensively, the success rate of samples can reach more than 60%.

## 4.2 Optical measurements

The transmitted power and the far-field intensity distributions under LP, RCP and LCP illumination to verify the high-efficiency and broadband PSHE are measured by the experimental setup shown in Figure 4F. In this configuration, a continuous wave solid-state laser emitting at desired wavelength is employed. The collimated beam passing through a linear polarizer and a quarter-waveplate ( $\lambda/4$ ) to generate the input light with desired polarization is normally incident to the metasurface for each measurement. The far-field intensity distributions are captured by a charge-coupled device mounted on a rotation stage. The incident and transmitted powers are measured by a Si photodiode (Thorlabs PM120VA). The incident power is normalized to the power passing through a quartz substrate.

**Acknowledgments:** This work was financially supported by the National Key R&D Program of China (Grant No. 2016YFA0200800 and 2016YFA0200400), the Natural Science Foundation of China (NSFC) (Grant Nos. 61771402, 11674266, 11674387, 11574369, 91323304, 11574368, 11574385 and 61888102), the Key Research Program of Frontier Sciences of CAS (Grant No. QYZDJ-SSW-SLH042), Science, Technology and Innovation Commission of Shenzhen Municipality (Grant No. JCYJ20170817162221169), the Hong Kong Scholars Program (XJ2017006).

**Author contribution:** All the authors have accepted responsibility for the entire content of this submitted manuscript and approved submission.

**Research funding:** This work was financially supported by the National Key R&D Program of China (Grant No. 2016YFA0200800 and 2016YFA0200400), the Natural Science Foundation of China (NSFC) (Grant Nos. 61771402, 11674266, 11674387, 11574369, 91323304, 11574368, 11574385 and 61888102), the Key Research Program of Frontier Sciences of CAS (Grant No. QYZDJ-SSW-SLH042), Science, Technology and Innovation Commission of Shenzhen Municipality (Grant No. JCYJ20170817162221169), the Hong Kong Scholars Program (XJ2017006).

**Conflict of interest statement:** The authors declare no conflicts of interest regarding this article.

## References

- [1] K. Y. Bliokh, F. J. Rodriguez-Fortuno, F. Nori, and A. V. Zayats, "Spin-orbit interactions of light," *Nat. Photon.*, vol. 9, p. 796, 2015.
- [2] M. I. Dyakonov and V. I. Perel, "Optical orientation in a system of electrons and lattice nuclei in semiconductors - theory," *Zh. Eksp. Teor. Fiz.*, vol. 65, p. 362, 1973.
- [3] J. E. Hirsch, "Spin Hall effect," *Phys. Rev. Lett.*, vol. 83, p. 1834, 1999.
- [4] O. Hosten and P. G. Kwiat, "Observation of the spin Hall effect of light via weak measurements," *Science*, vol. 319, p. 787, 2008.
- [5] Y. Qin, Y. Li, H. He, and Q. Gong, "Measurement of spin Hall effect of reflected light," *Optic Lett.*, vol. 34, p. 2551, 2009.
- [6] N. Shitrit, I. Bretner, Y. Gorodetski, V. Kleiner, and E. Hasman, "Optical spin Hall effects in plasmonic chains," *Nano Lett.*, vol. 11, p. 2038, 2011.
- [7] X. H. Ling, X. X. Zhou, X. N. Yi, et al., "Giant photonic spin hall effect in momentum space in a structured metamaterial with spatially varying birefringence," *Light Sci. Appl.*, vol. 4, no. 5, p. e290, 2015.
- [8] S. Y. Xiao, J. R. Wang, F. Liu, S. Zhang, X. B. Yin, and J. S. Li, "Spin-dependent optics with metasurfaces," *Nanophotonics*, vol. 6, p. 215, 2017.
- [9] X. B. Yin, Z. L. Ye, J. S. Rho, Y. Wang, and X. Zhang, "Photonic spin Hall effect at metasurfaces," *Science*, vol. 339, p. 1405, 2013.
- [10] J. X. Zhou, H. L. Qian, G. W. Hu, H. L. Luo, S. C. Wen, and Z. W. Liu, "Broadband photonic spin hall meta-lens," *ACS Nano*, vol. 12, no. 1, pp. 82–88, 2018.
- [11] J. Zhou, H. Qian, C. Chen, et al., "Optical edge detection based on high-efficiency dielectric metasurface," *Proc. Natl. Acad. Sci. U.S.A.*, vol. 116, no. 23, pp. 11137–11140, 2019.
- [12] J. B. Pendry, "Negative refraction makes a perfect lens," *Phys. Rev. Lett.*, vol. 85, p. 3966, 2000.
- [13] J. B. Pendry, A. J. Holden, D. J. Robbins, and W. J. Stewart, "Low frequency plasmons in thin-wire structures," *J. Phys. Condens. Matter*, vol. 10, p. 4785, 1998.

- [14] J. B. Pendry, A. J. Holden, D. J. Robbins, and W. J. Stewart, "Magnetism from conductors and enhanced nonlinear phenomena," *IEEE Trans. Microw. Theor. Tech.*, vol. 47, p. 2075, 1999.
- [15] D. Schurig, J. J. Mock, B. J. Justice, et al., "Metamaterial electromagnetic cloak at microwave frequencies," *Science*, vol. 314, p. 977, 2006.
- [16] R. A. Shelby, D. R. Smith, S. Schultz, et al., "Experimental verification of a negative index of refraction," *Science*, vol. 292, p. 77, 2001.
- [17] A. Cerjan and S. H. Fan, "Achieving arbitrary control over pairs of polarization states using complex birefringent metamaterials," *Phys. Rev. Lett.*, vol. 118, p. 253902, 2017.
- [18] M. Decker, M. Ruther, C. E. Kriegler, et al., "Strong optical activity from twisted-cross photonic metamaterials," *Optic Lett.*, vol. 34, pp. 2501–2503, 2009.
- [19] J. K. Gansel, M. Thiel, M. S. Rill, et al., "Gold helix photonic metamaterial as broadband circular polarizer," *Science*, vol. 325, pp. 1513–1515, 2009.
- [20] N. K. Grady, J. E. Heyes, D. R. Chowdhury, et al., "Terahertz metamaterials for linear polarization conversion and anomalous refraction," *Science*, vol. 340, pp. 1304–1307, 2013.
- [21] J. Hao, Y. Yuan, L. Ran, et al., "Manipulating electromagnetic wave polarizations by anisotropic metamaterials," *Phys. Rev. Lett.*, vol. 99, 2007, Art no. 063908.
- [22] C. Huang, Y. J. Feng, J. M. Zhao, Z. B. Wang, and T. Jiang, "Asymmetric electromagnetic wave transmission of linear polarization via polarization conversion through chiral metamaterial structures," *Phys. Rev. B*, vol. 85, p. 195131, 2012.
- [23] C. Wu, H. Q. Li, X. Yu, F. Li, H. Chen, and C. -T. Chan, "Metallic helix array as a broadband wave plate," *Phys. Rev. Lett.*, vol. 107, p. 177401, 2011.
- [24] P. C. Wu, W. Y. Tsai, W. T. Chen, et al., "Versatile polarization generation with an aluminum plasmonic metasurface," *Nano Lett.*, vol. 17, pp. 445–452, 2017.
- [25] F. Aieta, M. A. Kats, P. Genevet, and F. Capasso, "Multiwavelength achromatic metasurfaces by dispersive phase compensation," *Science*, vol. 347, pp. 1342–1345, 2015.
- [26] H. -T. Chen, A. J. Taylor, and N. F. Yu, "A review of metasurfaces: physics and applications," *Rep. Prog. Phys.*, vol. 79, 2016, Art no. 076401.
- [27] P. Genevet, F. Capasso, F. Aieta, M. Khorasaninejad, and R. Devlin, "Recent advances in planar optics: from plasmonic to dielectric metasurfaces," *Optica*, vol. 4, pp. 139–152, 2017.
- [28] S. Glybovski, S. A. Tretyakov, P. A. Belov, Y. S. Kivshar, and C. R. Simovski, "Metasurfaces: from microwaves to visible," *Phys. Rep.-Rev. Sect. Phys Lett.*, vol. 634, pp. 1–72, 2016.
- [29] M. Khorasaninejad and F. Capasso, "Metalenses: versatile multifunctional photonic components," *Science*, vol. 358, 2017, <https://doi.org/10.1126/science.aam8100>.
- [30] X. J. Ni, A. V. Kildishev, and V. M. Shalaev, "Metasurface holograms for visible light," *Nat. Commun.*, vol. 4, 2013, <https://doi.org/10.1038/ncomms3807>.
- [31] A. Shaltout, V. M. Shalaev, and M. L. Brongersma, "Spatiotemporal light control with active metasurfaces," *Science*, vol. 364, p. 6441, 2019.
- [32] S. L. Sun, Q. He, S. Y. Xiao, Q. Xu, X. Li, and L. Zhou, "Gradient-index meta-surfaces as a bridge linking propagating waves and surface waves," *Nat. Mater.*, vol. 11, pp. 426–431, 2012.
- [33] S. L. Sun, K. Y. Yang, C. M. Wang, et al., "High-efficiency broadband anomalous reflection by gradient meta-surfaces," *Nano Lett.*, vol. 12, pp. 6223–6229, 2012.
- [34] W. Zhu, Y. C. Fan, C. Li, et al., "Realization of near-infrared active fano-resonant asymmetric metasurface by precisely controlling the phase transition of Ge<sub>2</sub>Sb<sub>2</sub>Te<sub>5</sub>," *Nanoscale*, vol. 12, pp. 8758–8767, 2020.
- [35] N. F. Yu and F. Capasso, "Flat optics with designer metasurfaces," *Nat. Mater.*, vol. 13, pp. 139–150, 2014.
- [36] N. F. Yu, P. Genevet, M. A. Kats, et al., "Light propagation with phase discontinuities: generalized laws of reflection and refraction," *Science*, vol. 334, pp. 333–337, 2011.
- [37] G. X. Zheng, H. Muhlenbernd, M. Kenney, G. X. Li, T. Zentgraf, and S. Zhang, "Metasurface holograms reaching 80% efficiency," *Nat. Nanotechnol.*, vol. 10, pp. 308–312, 2015.
- [38] A. Arbabi, Y. Horie, M. Bagheri, and A. Faraon, "Dielectric metasurfaces for complete control of phase and polarization with subwavelength spatial resolution and high transmission," *Nat. Nanotechnol.*, vol. 10, pp. 937–943, 2015.
- [39] S. Jahani and Z. Jacob, "All-dielectric metamaterials," *Nat. Nanotechnol.*, vol. 11, pp. 23–26, 2016.
- [40] M. Khorasaninejad and K. B. Crozier, "Silicon nanofin grating as a miniature chirality-distinguishing beam-splitter," *Nat. Commun.*, vol. 5, p. 5386, 2014.
- [41] K. Koshelev, S. Kruk, E. V. Melik-Gaykazyan, et al., "Subwavelength dielectric resonators for nonlinear nanophotonics," *Science*, vol. 367, pp. 288–292, 2020.
- [42] Y. Li, S. Kita, P. Munoz, et al., "On-chip zero-index metamaterials," *Nat. Photon.*, vol. 9, pp. 738–742, 2015.
- [43] D. M. Lin, P. Y. Fan, E. Hasman, and M. L. Brongersma, "Dielectric gradient metasurface optical elements," *Science*, vol. 345, pp. 298–302, 2014.
- [44] M. I. Shalaev, J. B. Sun, A. Tsukernik, A. Pandey, K. Nikolskiy, and N. M. Litchinitser, "High-efficiency all-dielectric metasurfaces for ultracompact beam manipulation in transmission mode," *Nano Lett.*, vol. 15, pp. 6261–6266, 2015.
- [45] B. Wang, F. L. Dong, Q. T. Li, et al., "Visible-Frequency dielectric metasurfaces for multiwavelength Achromatic and highly dispersive holograms," *Nano Lett.*, vol. 16, pp. 5235–5240, 2016.
- [46] Y. M. Yang, I. I. Kravchenko, D. P. Briggs, et al., "All-dielectric metasurface analogue of electromagnetically induced transparency," *Nat. Commun.*, vol. 5, p. 5753, 2014.
- [47] Q. Zhao, J. Zhou, F. L. Zhang, et al., "Mie resonance-based dielectric metamaterials," *Mater. Today*, vol. 12, pp. 60–69, 2009.
- [48] M. Khorasaninejad, W. -T. Chen, R. C. Devlin, J. Oh, A. Y. Zhu, and F. Capasso, "Metalenses at visible wavelengths: diffraction-limited focusing and subwavelength resolution imaging," *Science*, vol. 352, pp. 1190–1194, 2016.
- [49] R. C. Devlin, M. Khorasaninejad, W. -T. Chen, J. Oh, and F. Capasso, "Broadband high-efficiency dielectric metasurfaces for the visible spectrum," *Proc. Natl. Acad. Sci. U.S.A.*, vol. 113, pp. 10473–10478, 2016.
- [50] W. -T. Chen, A. Y. Zhu, V. Sanjeev, et al., "A broadband achromatic metalens for focusing and imaging in the visible," *Nat. Nanotechnol.*, vol. 13, pp. 220–226, 2018.

- [51] R. C. Devlin, A. Ambrosio, N. A. Rubin, et al., “Arbitrary spin-to-orbital angular momentum conversion of light,” *Science*, vol. 358, pp. 896–901, 2017.
- [52] Y. Q. Hu, L. Li, Y. J. Wang, et al., “Trichromatic and tripolarization-channel holography with noninterleaved dielectric metasurface,” *Nano Lett.*, vol. 20, pp. 994–1002, 2020.
- [53] P. C. Huo, C. Zhang, W. Q. Zhu, et al., “Photonic spin-multiplexing metasurface for switchable spiral phase contrast imaging,” *Nano Lett.*, vol. 20, pp. 2791–2798, 2020.
- [54] H. Hsiao, C. H. Chu, D. -P. Tsai, F. Ding, A. Pors, and S. I. Bozhevolnyi, “Fundamentals and applications of metasurfaces,” *Small Methods*, vol. 1, 2017, Art no. 1600064.

---

**Supplementary Material:** The online version of this article offers supplementary material (<https://doi.org/10.1515/nanoph-2020-0290>).